TFEC-2020-31576

THE SWIRLING MOTION OF DRIBBLING HONEY

Majid Molki*

Southern Illinois University Edwardsville, Edwardsville, IL 62026, USA

ABSTRACT

Viscous liquids falling onto a flat surface may experience flow instability and swirling motion. For a certain set of parameters, liquids such as raw honey, silicone oil, heavy syrup, and many other high-viscosity liquids exhibit swirling and coiling behavior. In this investigation, I have considered falling and swirling motion of wildflower honey dribbled from a certain height onto a surface. Honey is a non-Newtonian fluid whose rheological behavior is implemented by the power-law model. The computational approach used in this work is based on finite-volume and volume-of-fluid (VOF) methods. The model is unsteady and three dimensional. Computations performed with three samples of wildflower honey reveal flow instability and swirling motion as it lands on a hard surface. Several new observations such as the sense of rotation, the effect of honey samples on the swirls, the possible role of vorticity magnitude and components on the onset of swirls are presented and discussed.

KEYWORDS: Honey, Swirling, Coiling, Liquid thread, Rope coiling, Non-Newtonian, Rheology, Vorticity.

1. INTRODUCTION

A thin stream of very viscous liquid falling slowly from a certain height shows a remarkable swirling motion and a helical structure before landing on a surface. This observation is familiar when honey is poured onto a toast at the breakfast table. Other liquids such as silicone oils have been used as a test fluid to create such flow features in a laboratory. The folding behavior of a stream of shampoo and shave gels are other familiar examples. However, not every viscous liquid may reveal the swirling motion and a helical structure. It is hard to create conditions for the common household liquids such as cooking oil and olive oil to demonstrate this physical behavior.

There are many experimental and computational results on the whirling helical structure of thin streams of viscous liquids in the published literature. One of the earlier experiments [1] measured the frequency of coiling for different fall heights using transmission oil. While the liquid filament rotates about the vertical axis and forms a conical coil at the bottom, the liquid particles, including the particles on the cone, do not rotate about this axis. The liquid ejected from the injection site advances downward along a vertical line until near the landing surface it becomes unstable. This leads into a lateral swinging motion like a pendulum which then begins the onset of coiling.

The familiar buckling phenomenon when the maximum axial load on a column exceeds a critical limit is another view of this problem. Theoretical studies have indicated that the axial compression and a critical fall distance brings instability to a thin liquid impinging upon a surface [2]. In this sense, the current problem is

*Corresponding Author: mmolki@siue.edu

the fluid dynamics counterpart of the buckling instability of thin elastic rods. Other related phenomena are the folding of viscous sheets, such as molten chocolate and cake batter, and coiling of elastic ropes.

In the past two decades, several detailed analytical, experimental, and computational investigations of this problem have appeared in the published literature [3-10]. At lower fall heights the liquid filament is still an axial stretching flow similar to the classical stagnation point flow. As the fall height increases, the bending disturbances make the flow unstable. Scaling laws predict the coiling frequency of the filament in terms of filament radius and flow rate [3,4]. Smaller filament radii lead to higher coiling frequencies.

Because they are very thin, liquid filaments allow the transformation of the unsteady, three-dimensional Navier-Stokes equations to the steady, one-dimensional equations that describe the dynamics of a curved line [6]. This method has successfully predicted special features of the flow including the frequency of oscillations. However, a major drawback is that the liquid stream must remain sufficiently thin to be represented by a curved line. As the liquid stream touches the landing surface and a spiral coil is formed, the filament loses its identity and the model is not applicable anymore.

This paper aims to model the swirling motion of a thin stream of wildflower honey. The computational model employs the unsteady three-dimensional Navier-Stokes equations for laminar flow. Honey is a shear-thinning, non-Newtonian liquid and is modeled as such in this paper. Many papers have been published on liquid coiling, but, except for a recent work by the author [11], the number of numerical publications on this topic using the current approach is scarce.
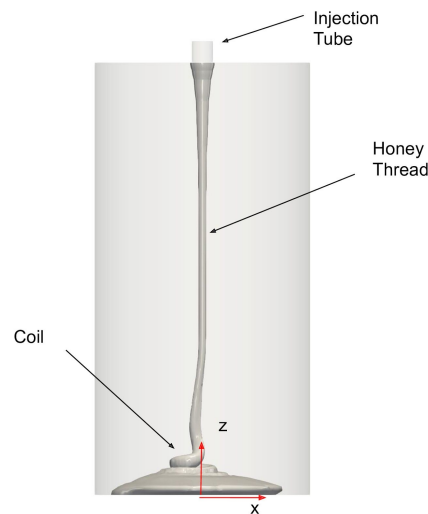

Fig. 1 A thin stream of honey emerging from a short injection tube forms a filament that falls swirling onto a flat surface. The noteworthy features of the flow are the larger diameter of the steam at the top, thinness in the middle, whirling and twisting motion at the bottom, and spreading of liquid over the surface. Flow rate, tube diameter, and the fall height are $Q = 9.82 \times 10^{-9}$ m^3/s, $d = 0.005$ m, and $h = 0.1$ m, respectively.

2. THE MATHEMATICAL FORMULATION

2.1 Geometry   Figure 1 shows a typical image generated by a current simulation. Honey emerges from a small tube located 0.1 m above the bottom surface. The tube diameter and length are both equal to 0.005 m. The surrounding air envelopes the falling honey, and the gravity stretches the filament to thinner diameters. Before landing on the bottom surface, the unstable filament bends and starts whirling. Unlike very viscous fluids that construct a rising helical coil at the bottom [12], honey puddles and spreads out over the surface.

2.2 The Equations The coiling filament is unsteady and three dimensional. The flow field involves two phases -- liquid (honey) and gas (air). Besides, the rheological features of honey classify it as a non-Newtonian fluid. The proper mathematical formulation for this problem involves the conservation of mass (continuity) and momentum (Navier-Stokes) in unsteady and three-dimensional form. Also, a constitutive equation for the non-Newtonian fluid relates viscous stresses to the rate of deformation. Furthermore, an equation for the liquid volume fraction tracks the liquid-gas interface. Using Cartesian tensor notation, these equations for laminar incompressible flow are summarized below [13].

Continuity
$$\frac{\partial u_i}{\partial x_i} = 0 \tag{1}$$

Navier-Stokes
$$\frac{\partial(\rho u_i)}{\partial t} + \frac{\partial(\rho u_j u_i)}{\partial x_j} = -\frac{\partial p}{\partial x_i} + \frac{\partial \tau_{ij}}{\partial x_j} + \rho g_i + f_i \tag{2}$$

Non-Newtonian (power-law)
$$\tau_{ij} = 2\mu_{eff}S_{ij}, \ \mu_{eff} = K_t\dot{\gamma}^{n-1}, \ \dot{\gamma} = \sqrt{2}S = \sqrt{2S_{ij}S_{ij}},$$
$$S_{ij} = \frac{1}{2}(\frac{\partial u_j}{\partial x_i} + \frac{\partial u_i}{\partial x_j}) \tag{3}$$

Liquid volume fraction
$$\frac{\partial \alpha}{\partial t} + \frac{\partial(\alpha u_i)}{\partial x_i} + \frac{\partial}{\partial x_i}(\alpha(1-\alpha)u_{c_i}) = 0 \tag{4}$$

Surface tension force
$$f_i = \sigma\kappa\frac{\partial \alpha_c}{\partial x_i}, \ \kappa = -\frac{\partial n_i}{\partial x_i}$$
$$\alpha_c = \frac{1}{1-C_c}[min(max(\alpha, \frac{C_c}{2}), 1 - \frac{C_c}{2}) - \frac{C_c}{2}] \tag{5}$$

In these equations, repeated indices imply summation. The index i = 1, 2, 3 refers to the coordinates $x_i = x_1$, x_2, x_3, corresponding to the conventional coordinates x, y, and z.

2.3 The Non-Newtonian Model Honey is a non-Newtonian fluid represented by a power-law equation.

$$\tau = K_t\dot{\gamma}^n \tag{6}$$

The shear stress, τ, and shear rate, $\dot{\gamma}$, are determined from viscometer readings. Using the least-squares fit to the data, the flow consistency index, K_t, and flow behavior index, n, are determined. The values of K_t and n in the present work are taken from the experimental measurements of reference [14].

The power-law equation is rearranged and written in terms of effective viscosity.

$$\tau = K_t\dot{\gamma}^{n-1}\dot{\gamma} = \mu_{eff}\dot{\gamma} \tag{7}$$

Therefore, the effective viscosity in terms of viscometer shear rate may be obtained from

$$\mu_{eff} = K_t \dot{\gamma}^{n-1} \tag{8}$$

This viscosity may now be used in Eq. (3) to obtain the viscous stress tensor for Eq. (2).

$$\tau_{ij} = 2\mu_{eff} S_{ij} \tag{9}$$

Equation (9) looks very similar to the equation $\tau_{ij} = 2\mu S_{ij}$ for Newtonian fluids.

Effective viscosity, μ_{eff}, depends not only on constants K_t and n, but it also depends on the simple shear rate, $\dot{\gamma}$, applied by the viscometer. It can be shown that

$$\dot{\gamma} = \sqrt{2}S = \sqrt{2S_{ij}S_{ij}} \tag{10}$$

It is noted that the shear rate $\dot{\gamma}$ obtained from the viscometer measurement is not equal to the magnitude (S) of the rate of deformation tensor (S_{ij}). Flow in a viscometer is a simple shear flow with $\dot{\gamma} = du_1/dx_2 = u_1/x_2$. To relate $\dot{\gamma}$ to S, consider the square of the magnitude of the rate of deformation tensor.

$$S^2 = S_{ij}S_{ij} = \frac{1}{2}(\partial_i u_j + \partial_j u_i)\frac{1}{2}(\partial_i u_j + \partial_j u_i) \tag{11}$$

For the simple shear flow, only u_1 and the derivative with respect to x_2 are not zero. The equation is then expanded and simplified.

$$S^2 = \frac{1}{4}(\partial_i u_j \partial_i u_j + \partial_i u_j \partial_j u_i + \partial_j u_i \partial_i u_j + \partial_j u_i \partial_j u_i) = \frac{1}{2}(\partial_2 u_1)^2 = \frac{1}{2}\dot{\gamma}^2 \tag{12}$$

This equation confirms that the relationship between the simple shear rate and the magnitude of the rate of deformation tensor is $\dot{\gamma} = \sqrt{2}S = \sqrt{2S_{ij}S_{ij}}$, as stated earlier.

In this investigation, honey is a power-law fluid, but the air is Newtonian, i.e., $\tau_{ij} = 2\mu S_{ij}$.

2.4 The Filtered Volume Fraction Gradient of the liquid volume fraction used in computing the surface tension force is sensitive to data noise. Prediction of the surface tension force may be improved if the volume fraction is filtered before the gradient is calculated. The filtered liquid volume fraction, α_c, is evaluated according to Eq. (5) [15].

2.5 Boundary Conditions The boundaries of the solution domain consist of the tube inlet (diameter d = 0.005 m, located at z = 0.105 m above the bottom surface), tube surface (a cylinder of diameter d = 0.005 m and length 0.005 m), top wall (an annulus of diameters 0.005 m and 0.05 m), bottom wall (a circular surface of diameter 0.05 m), and lateral cylindrical surface (diameter 0.05 m and length 0.1 m).

Velocity at the boundaries: Velocity at the tube inlet is (0,0,-0.0005) m/s. No-slip boundary condition is applied to all walls. The velocity gradient at the cylindrical boundary of the domain is zero.

The pressure at the boundaries: In the computations, the hydrostatic pressure is subtracted from the static pressure to define the new pressure, $p_{\rho gh}$.

$$p_{\rho gh} = p - \rho gh \qquad (13)$$

The boundary condition is applied to $p_{\rho gh}$. At the tube inlet, the gradient of this pressure is zero. The pressure gradient is also zero on all solid walls. The magnitude of pressure is 0 Pa on the outflow section, i.e., on the larger cylindrical surface.

Liquid volume fraction at the boundaries: At the tube inlet, the liquid volume fraction is equal to 1, meaning that only liquid enters the computational domain. The gradient of liquid volume fraction is zero on all solid walls. The gradient of the volume fraction is zero on the cylindrical surface (outflow). If a reverse flow occurs at the outflow, the liquid volume fraction of the entering fluid will be zero, i.e., only air can enter the domain from outside.

3. COMPUTATIONAL APPROACH

The computations were performed using the finite-volume method and the open-source software, OpenFOAM. The computational mesh is nonuniform, unstructured, and mostly deployed in and around the core region where the liquid thread descends. With parallel computing on four cores in a single computing component (chip), it took about 20 hours of clock time to achieve 40 seconds of the simulation time. As the simulation images indicate, the total time was sufficient to allow the liquid filament to go through the initial transients and establish a repeatable pattern.

The governing equations are discretized using a second-order method for the convective and diffusive terms. The time derivative is approximated using the Crank-Nicolson method. The PIMPLE algorithm, which is a hybrid approach consisting of PISO and SIMPLE algorithms, provides the link between velocity and pressure. The computations are carried out to within a residual tolerance of 10^{-8} for the liquid volume fraction, and 10^{-6} for the fluid velocity and pressure. The computations have a variable time-step with a Courant number of 0.75. This value of the Courant number ensures that the computations are stable. The computations continued for 40 seconds of simulation time.

In a previous investigation [11] with a similar approach, three variables, namely, liquid volume fraction, fluid pressure, and magnitude of velocity, were selected to indicate whether the discretization errors decrease with mesh refinement. The results are available in reference [11] and will not be repeated here. The grid refinement showed that the distributions of these variables approach a limiting case, implying that the discretization errors are diminishing.

4. DIMENSIONLESS PARAMETERS

Using the Buckingham π theorem, four major dimensionless parameters are listed in reference [16], excluding the surface tension. If the surface tension is included, the Bond number becomes the fifth dimensionless parameter to describe the present problem.

$$\Omega(\frac{\nu}{g^2})^{1/3}, \; H(\frac{g}{\nu^2})^{1/3}, \; Q(\frac{g}{\nu^5})^{1/3}, \; d(\frac{g}{\nu Q})^{1/4}, \; \frac{\rho g d^2}{\sigma} \tag{14}$$

The Bond number, Bo = $\rho g d^2/\sigma$, in this investigation is large and equal to 2966, indicating that the surface tension force is negligible. The first dimensionless parameter, $\square(\nu/g^2)^{1/3}$, is not reported here due to the limited range of parameters.

Table 1 shows the parameters for the honey samples modeled in this investigation. To identify each sample, an identification code is given in the second column of the table. The codes are the same as those listed in reference [14]. As stated in [14], rheological measurements for each sample were carried out in a concentric-type rotational viscometer. Three out of seven samples from reference [14] are selected at two different temperatures. The experimental values of the flow consistency index, K_t and flow behavior index, n, as well as the density and dimensionless parameters are given in the table. The range of variables considered in this investigation, and the range of corresponding dimensionless parameters, are limited. Studies with other fluids for a wider range are available in the literature [3,10,16].

Table 1 Samples of honey and values of dimensional and dimensionless parameters used in this investigation. The identification codes in the second column are the same as those listed in reference [14].

Fluid	Code [14]	T, C	K_t, Pa.s^n	n	ρ, kg/m^3	$\pi_H = H(\frac{g}{\nu^2})^{1/3}$	$\pi_Q = Q(\frac{g}{\nu^5})^{1/3}$	$\pi_d = d(\frac{g}{\nu Q})^{1/4}$
Honey 1	GD	38	37.7	0.60	1300	2.27	7.68E-6	2.15
Honey 1	GD	58	41.5	0.28	1300	2.13	6.54E-6	2.10
Honey 2	GF	38	46.5	042	1246	1.92	5.04E-6	2.02
Honey 2	GF	58	41.9	0.27	1245	2.05	6.00E-6	2.08
Honey 3	GY	38	43.9	0.39	1328	1.81	4.38E-6	1.98
Honey 3	GY	58	36.3	0.29	1328	2.36	8.47E-6	2.19

5. RESULTS AND DISCUSSION

5.1 The Gravitational Effect At the outset, the flow was simulated to find out the effect of gravity on the stability of the falling liquid. For gravity values of 0.1g, g, and 10g, where g = 9.81 m/s², the flow of honey filament is shown in Fig. 2. The colors represent the magnitude of the local fluid velocity. It is seen that honey accelerates before decelerating to the stagnation point on the impingement surface. Obviously, the acceleration is faster at higher values of gravity. Flow is stable and the filament does not show any sign of swirling and whirling.

5.2 The Swirling Motion If the honey is injected at 0.0005 m/s (100 times slower than that in Fig. 2), the falling filament will experience flow instability and the honey starts swirling as pictured in Fig. 3. The time of these images from left to right is from 38.8 to 40 s in 0.4-second intervals. The dribbling honey is along a straight line until, near the bottom surface, it becomes unstable and starts swirling. Unlike the liquids tested in reference [12], honey is not so viscous to support the weight of a rising coil. Instead, it puddles and spreads over the surface.
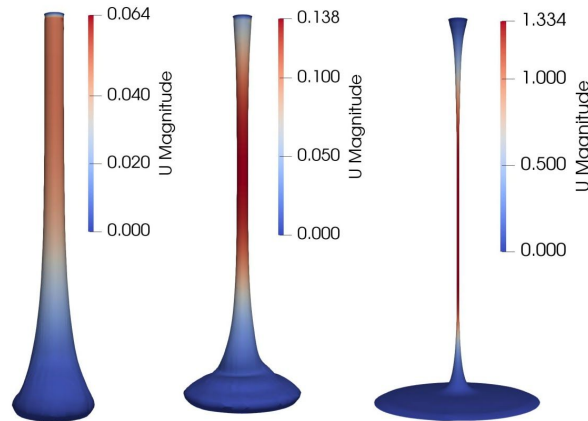
Fig. 2 The effect of gravity on the stability of the downward flow of honey. From left to right, gravity is 0.1g, g, and 10g; flow speed at the tube inlet is 0.05 m/s for each of the three cases, corresponding to a flow rate of 9.82×10^{-7} m^3/s. The color bars define the magnitude of the local velocity in each case.
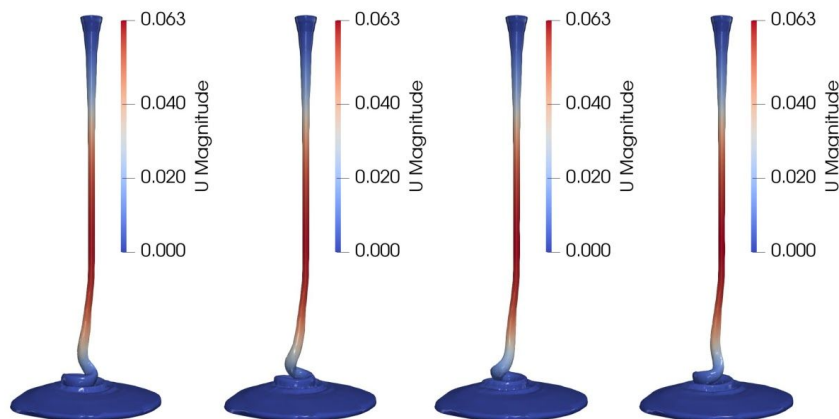

Fig. 3 The swirling of honey filament. From left to right, the images correspond to 38.8 s to 40 s with 0.4 s intervals. Flow speed at the tube inlet is 0.0005 m/s corresponding to a flow rate of 9.82×10^{-9} m^3/s. The colors indicate the magnitude of velocity. The fall speed is faster in the middle. The filament decelerates before the onset of swirling.

A noteworthy feature of the images in Fig. 3 is the sense of rotation. Using the right-hand rule, the liquid filament in this figure is swirling in the positive direction of the z-axis. However, there is no reason for the swirling to be positive. Table 2 presents the sense of rotation for all cases listed in Table 1 and an additional repeat case. These results indicate that the sense of rotation may be positive or negative, even though the mesh used in all cases is the same.

The images available in the published literature confirm that swirling is not always in the same direction. In reference [1], the sense of rotation in experiments with SAE 140 at 27.5 °C and flow rate of 0.0810×10^{-6} m^3/s is positive for the fall heights of 0.042 m and 0.203 m, but it is negative for the fall height of 0.125 m. In reference [3], a photograph of a thin filament of silicone oil shows a regular helical coil with a positive sense of swirl. In reference [12], photographs of silicone oil dribbled onto a metal plate at different heights show

both positive and negative senses. These experimental observations for the direction of swirling are consistent with the predictions of the present computations.

Table 2 Summary of sense of rotation. Positive (+) means the swirling is in the positive direction of the z-axis and negative (-) refers to the negative z-direction.

Fluid	Code [14]	T, C	K_t, Pa.s^n	n	ρ, kg/m^3	Sense of Swirl
Honey 1	GD	38	37.7	0.60	1300	+
Honey 1 (Repeat)	GD	38	37.7	0.60	1300	-
Honey 1	GD	58	41.5	0.28	1300	+
Honey 2	GF	38	46.5	042	1246	+
Honey 2	GF	58	41.9	0.27	1245	+
Honey 3	GY	38	43.9	0.39	1328	-
Honey 3	GY	58	36.3	0.29	1328	-

Figure 4 is a top view of the coiling depicted in Fig. 3. The images are colored to show the magnitude of the flow speed. It is clear from the figure that coiling is faster than other parts of the flow. Also, the coiling has a positive sense of rotation, i.e., the filament is rotating in the +z direction. After impinging on the bottom surface, honey spreads over the surface. Other investigators have shown that very viscous filaments form a rising coil that eventually tilts and tends to fall to the bottom surface [12]. The viscosity of the honey samples modeled in this investigation is not high enough to sustain a tall coil.
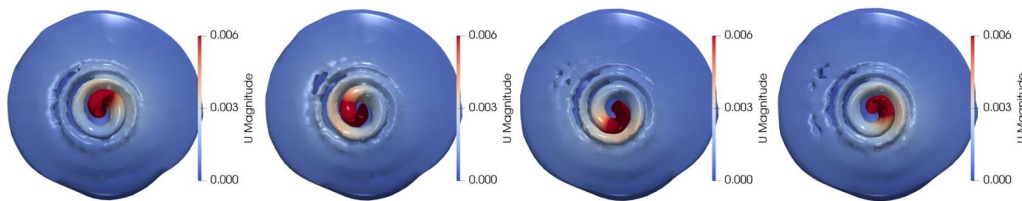

Fig. 4 Top view of the swirling filament. The frames correspond to the images in Fig. 3. From left to right, the frames correspond to 38.8 s to 40 s with 0.4-second intervals. Flow speed at the tube inlet is 0.0005 m/s, corresponding to a flow rate of 9.82×10^{-9} m^3/s. The colors indicate the magnitude of the local speed. The speed is faster on the filament in the middle. Coiling has a positive sense, i.e., the swirling is in the +z direction.

5.3 The Vorticity of the Swirling Filament In search of criteria related to filament instability and coiling, it is worthwhile to examine the role of fluid vorticity. Figure 5 is a presentation of vorticity magnitude and component $\square_x$ at 40 seconds. It is helpful to know that vorticity magnitude is given by a positive number, while the components may be positive or negative.
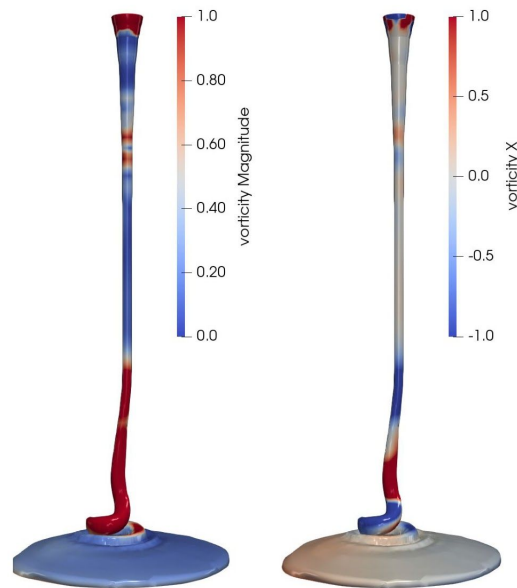
Fig. 5 Surface of the swirling filament is colored by vorticity magnitude (left) and vorticity component, $\square_x$. These images are captured at 40 s. Although the vorticity magnitude is positive, the component of vorticity may be positive or negative.

For the specific values of parameters in this investigation, the flow in Fig. 5 is unstable and swirling. But the question here is whether vorticity may be linked to the filament instability. Reference [16] uses dimensionless parameters on a regime diagram that permits the prediction of the coiling frequency. The values of dimensionless parameters depend on the values of dimensional parameters. Is there a relationship between the dimensionless parameters and vorticity? Can vorticity be used as a criterion for the onset of coiling? Unlike the dimensionless parameters which may be calculated from a knowledge of dimensional parameters, vorticity becomes available only after the flow field has been established.

According to Fig. 5, the lower part of the filament contains a strong vorticity magnitude and component. The local variation of the vorticity magnitude in this region of the filament is small, but the magnitude itself is large. However, the figure shows the component $\square_x$ varies greatly between negative and positive values. Large values of $\square_x$ and $\square_y$ have a tendency to bend the filament, making it susceptible to curving and coiling. The vertical component $\square_z$, on the other hand, goes with rotating and twisting the filament. Regardless of which component is in control, the presence of vorticity in the proximity of the coiling region is a noteworthy feature of the flow.

5.4 Variation of Parameters along the Vertical Axis A key location in the solution domain is the centerline along the positive z-axis. As seen in Fig. 6, the liquid volume fraction is changing along the axis. The abscissa range is from the bottom plate (z = 0) to the injection site (z = 0.1 m). For a straight stable filament, the vertical centerline is covered entirely with liquid ($\alpha = 1$). However, the swirling motion, which mainly occurs near the bottom surface, takes the liquid away from the axis. The variation of α in the upper portion of the filament is smooth.

Also shown in Fig. 6 is the fluid pressure along the positive z-axis. Unlike volume fraction, pressure changes rapidly near the injection site. The initial pressure rise due to surface tension is quickly followed by a rapid pressure drop due to fluid acceleration.

Velocity components u and v prevent the filament from moving downward in a straight line. Therefore, they promote the onset of instability and coiling. In Fig. 6, a large segment of the filament is free from lateral motion. However, the variations of u and v are quite visible further down in the lower half of the filament.

Vorticity indicates the local rotation of the fluid particles. The vorticity components ω_x, ω_y, and ω_z in Fig. 6 are negligibly small in the upper segment of the vertical axis indicating an irrotational flow within the filament. However, in the lower part of the axis, all three components of vorticity change rapidly. Since the vorticity is generated by the action of shear stresses, this plot confirms that the honey viscosity in this region plays an important role. It is not surprising that three of the dimensionless parameters introduced earlier contain the kinematic viscosity.
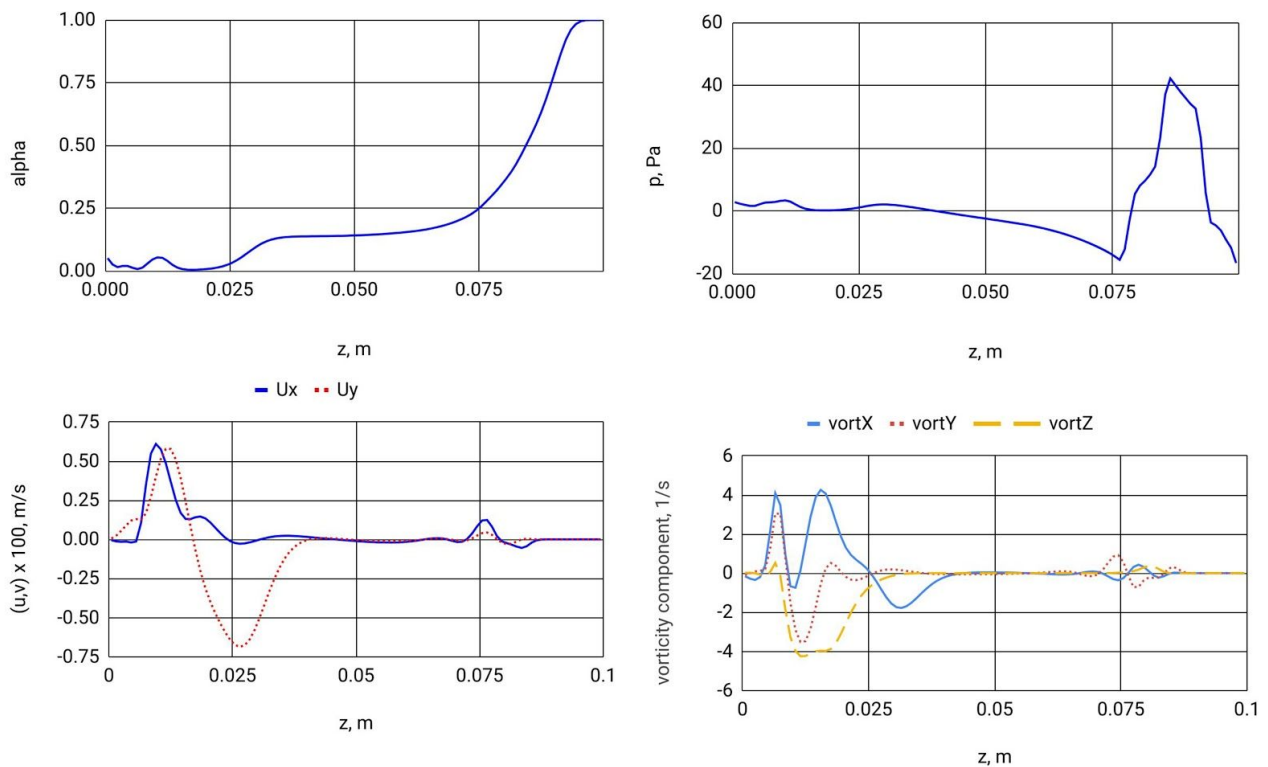
Fig. 6 Distribution of the liquid volume fraction, pressure, velocity components, and vorticity components along the vertical centerline (z-axis). The plots are for sample honey 1 (GD, 38°C) at 40 s.

5.5 The Swirling Motion of Honey Samples Images of three swirling honey samples are shown in Fig. 7. The initial flow acceleration, thinning of the filament, and swirling near the bottom surface are seen in all three cases. The overall look of the falling filament is nearly the same for the three samples. However, a closer look reveals some differences. It appears that the shape and the number of coils are slightly different from left to right, which may be due to different rheological properties.

6. CONCLUDING REMARKS

This computational study considers the swirling and coiling behavior of three samples of wildflower honey when dribbled from a certain height onto a flat surface. The model employs unsteady, three-dimensional

governing equations with the power-law model for the non-Newtonian honey and Newtonian model for the surrounding air. The honey-air interface is captured by the volume-of-fluid method in conjunction with a filtering procedure to damp out data noise for a more accurate surface tension force.
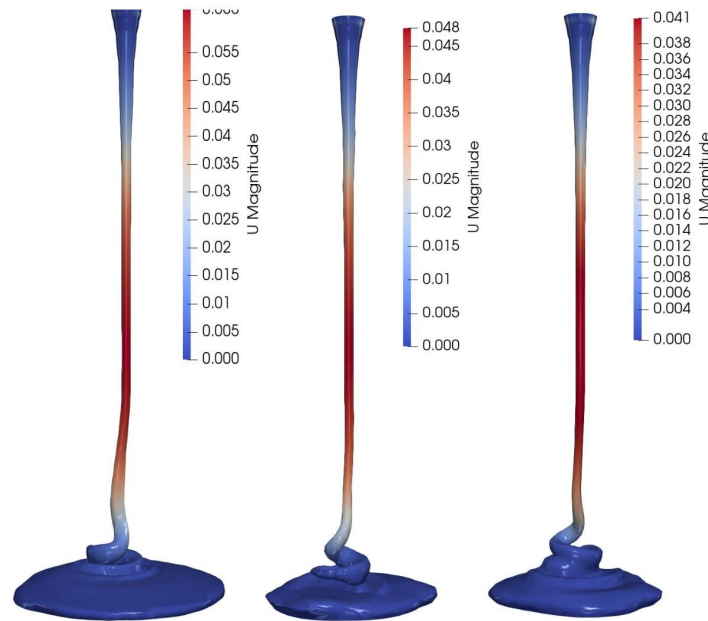

Fig. 7 The swirling motion of three honey samples at 40 s. From left to right, the images are for samples 1 (GD), 2 (GF), and 3 (GY) at 38°C. Flow speed at the tube inlet is 0.0005 m/s, corresponding to a flow rate of 9.82×10^{-9} m³/s. The colors indicate the local velocity magnitude.

At a higher injection speed of 0.05 m/s, swirling and coiling are absent. The thin filament flows vertically downward and decelerates to the stagnation point. The magnitude of gravitational acceleration does not change this flow pattern. At higher gravity, the filament is thinner.

The filament grows unstable and starts whirling at the lower injection speed of 0.0005 m/s. The sense (direction) of rotation is not known in advance, but in each simulation, the direction of rotation stays the same for the entire duration of the run.

Vorticity is abundant in the lower part of the filament. The magnitude of vorticity remains large in this region, and the large values continue toward the coil. Vorticity component ω_x is also high in this region, but it changes sign as the swirling continues. In addition to the vorticity component, velocity components u and also change rapidly in the swirling region.

Simulation of honey samples shows that they have similar flow features such as the initial acceleration, stretching of the filament, and swirling near the bottom surface, but they also reveal some differences which seem to be due to different rheological properties.

NOMENCLATURE

C_c	filter constant, 0.98	(-)	α	liquid volume fraction	(-)
f_i	surface tension force per unit	(N/m³)	α_c	filtered liquid volume fraction	(-)

volume, Eq. (2)

h	fall height, 0.1	(m)	$\dot{\gamma}$	shear rate	(s^{-1})
K_t	flow consistency index	Pa·s^n	κ	curvature, Eq. (5)	(m^{-1})
n	flow behavior index	(-)	u_{eff}	effective viscosity, Eq. (3)	(Pa·s)
S	magnitude of S_{ij}	(s^{-1})	σ	surface tension	(N/m)
S_{ij}	rate of deformation tensor, Eq. (3)	(s^{-1})	$\partial_i()$	partial derivative, $\partial()/\partial x_i$	(-)
VOF	volume of fluid				

REFERENCES

[1] Barnes, G., Woodcock, R., "Liquid rope-coil effect," American Journal of Physics, 26(4), pp. 205-209, (1958).

[2] Tchavdarov, B., Yarin, A. L., Radev, S., "Buckling of thin liquid jets," Journal of Fluid Mechanics, 253, pp. 593-615, (1993).

[3] Mahadevan, L., Ryu, W. S., Samuel, A. D. T., "Fluid 'rope trick' investigated," Nature, 392, p. 140, (1998).

[4] Mahadevan, L., Ryu, W. S., Samuel, A. D. T., "Correction: Fluid 'rope trick' investigated," Nature, 403, p. 502, (2000).

[5] Skorobogatiy, M., Mahadevan, L., "Folding of viscous sheets and filaments," Europhysics Letters, 52(5), pp. 532–538, (2000).

[6] Ribe, N. M., "Coiling of Viscous Jets," Proceedings: Mathematical, Physical and Engineering Sciences, vol. 460(2051), pp. 3223-3239, (2004).

[7] Maleki, M., Habibi, M., Golestanian, R., Ribe, N. M., Bonn, D., "Liquid rope coiling on a solid surface," Physical Review Letters, 21(93), 214502, pp. 1-4, (2004).

[8] Ribe, N. M., Habibi, M., Bonn, D., "Stability of liquid rope coiling," Physics of Fluids, 18, 084102, pp. 1-12, (2006).

[9] Ribe, N. M., Huppert, H. E., Hallworth, M. A., Habibi, M., Bonn, D., "Multiple coexisting states of liquid rope coiling," Journal of Fluid Mechanics, 555, pp. 275-297, (2006).

[10] Habibi, M., Maleki, M., Golestanian, R., Ribe, N. M., Bonn, D., "Dynamics of liquid rope coiling," Physical Review E, 74, 066306, pp. 1-10, (2006).

[11] Molki, M., "Liquid Rope Coiling with Multiple Viscous Jets," 4th Thermal and Fluids Engineering Conference, ASTFE Digital Library, DOI: 10.1615/TFEC2019.fli.027216, pp. 747-758, (2019).

[12] Ribe, N. M., Habibi, M., Bonn, D., "The liquid rope trick," Scientific American, February, pp.66-71, (2014).

[13] Panton, R. L, *Incompressible Flow,* 3rd ed, John Wiley, Hoboken, NJ, (2005).

[14] Al-Mahasneh, M. A., Rababah, T. M., Amer, M., Al-Omoush, M., "Modeling physical and rheological behavior of minimally processed wildflower honey," Journal of Food Processing and Preservation, 38, pp. 21-30, (2012).

[15] Shams, M., Raeini, A. Q., Blunt, M. J., Bijeljic, B. "A numerical model of two-phase flow at the micro-scale using the volume-of-fluid method," Journal of Computational Physics, 357, pp. 159-182, (2018).

[16] Ribe, N. M., "Liquid rope coiling: a synoptic view," Journal of Fluid Mechanics, 812(R2), pp. 1-10, (2017).